Energy & Environmental Science

PAPER

View Article Online
View Journal | View Issue

Cite this: *Energy Environ. Sci.*, 2014, **7**, 1685

Robust nanostructures with exceptionally high electrochemical reaction activity for high temperature fuel cell electrodes

WooChul Jung,[ab] Kevin L. Gu,[a] Yoonseok Choi[b] and Sossina M. Haile*[a]

Metal nanoparticles are of significant importance for chemical and electrochemical transformations due to their high surface-to-volume ratio and possible unique catalytic properties. However, the poor thermal stability of nano-sized particles typically limits their use to low temperature conditions (<500 °C). Furthermore, for electrocatalytic applications they must be placed in simultaneous contact with percolating ionic and electronic current transport pathways. These factors have limited the application of nanoscale metal catalysts (diameter <5 nm) in solid oxide fuel cell (SOFC) electrodes. Here we overcome these challenges of thermal stability and microstructural design by stabilizing metal nanoparticles on a scaffold of $Sm_{0.2}Ce_{0.8}O_{2-\delta}$ (SDC) films with highly porous and vertically-oriented morphology, where the oxide serves as a support, as a mixed conducting transport layer for fuel electro-oxidation reactions, and as an inherently active partner in catalysis. The SDC films are grown on single crystal YSZ electrolyte substrates by means of pulsed-laser deposition, and the metals (11 μg cm^{-2} of Pt, Ni, Co, or Pd) are subsequently applied by D.C. sputtering. The resulting structures are examined by TEM, SIMS, and electron diffraction, and metal nanoparticles are found to be stabilized on the porous SDC structure even after exposure to 650 °C under humidified H_2 for 100 h. A.C. impedance spectroscopy of the metal-decorated porous SDC films reveals exceptionally high electrochemical reaction activity toward hydrogen electro-oxidation, as well as, in the particular case of Pt, coking resistance when CH_4 is supplied as the fuel. The implications of these results for scalable and high performance thin-film-based SOFCs at reduced operating temperature are discussed.

Received 26th October 2013
Accepted 12th February 2014

DOI: 10.1039/c3ee43546f

www.rsc.org/ees

Broader context

Solid oxide fuel cells (SOFCs) provide unparalleled fuel-to-electric conversion efficiency across power scales, from a few milliwatts to hundreds of megawatts. A key barrier to widespread SOFC deployment has been high cost, in part attributable to the high temperature of operation, typically in the 800–1000 °C range. Lower temperature operation, in turn, has been hindered by poor electrocatalysis rates. Here we demonstrate SOFC anodes with unprecedented activity for both hydrogen and methane electro-oxidation at 600 °C. The innovation lies in the use of nanostructured ceria in combination with ultra-low loadings (11 μg cm^{-2}) of catalytic metals: Pt, Pd, Ni or Co. Despite the nanoscale features, the activity experiences negligible degradation over a continuous measurement period of 120 h. This work sets the stage for the adoption of high efficiency SOFCs for the cost-effective utilization of natural gas in electric power generation.

1. Introduction

The attractive combination of high conversion efficiency and fuel flexibility positions solid oxide fuel cells (SOFCs) to play a critical role in a carbon-neutral, sustainable energy future.[1] Currently, the main commercialization barrier of this technology is a prohibitive cost per unit power output, estimated at 750 $ per kW in 2010.[2] It is widely appreciated that SOFC costs can be substantially reduced by lowering operation temperatures, which enables the use of lower cost materials for auxiliary components and increases lifetimes.[3] However, at such reduced temperatures (<700 °C), electrochemical processes at both electrodes are sluggish and power output substantially decreases. This work focuses on strategies for enhancing activity of SOFC anodes at reduced temperatures. Although the cathode is commonly considered the performance limiting electrode, insufficient anode activity remains a challenge, particularly with the advent of high activity cobaltite cathodes.[4,5]

In recent years it has become recognized that composite SOFC anodes incorporating ceria as a component have substantially higher activity than those utilizing either only YSZ (yttria-stabilized zirconia) or only LSGM [$(La,Sr)(Ga,Mg)O_3$] as

---

[a] Materials Science, California Institute of Technology, Pasadena, CA 91125, USA. E-mail: smhaile@caltech.edu; Fax: +1 626-395-8868; Tel: +1 626-395-2958

[b] Department of Materials Science and Engineering, Korea Advanced Institute of Science and Engineering, Daejeon, 305-701, Republic of Korea. E-mail: wcjung@kasit.ac.kr; Fax: +82-42-350-3310; Tel: +82-42-350-3314

the oxide phase. While most studies of this effect are focused on hydrocarbon electro-oxidation,[6,7] the high activity of the ceria surface for hydrogen and the specific reaction, H_2 (gas) + $O^{2-} \rightarrow H_2O$ (gas) + $2e^-$ has been definitively demonstrated.[8,9] Thus, depending on the microstructural arrangement, both the oxide and the metal, typically Ni, which also serves to provide the predominant electronic pathway, contribute to electrocatalysis.

In parallel, it has become evident that addition of metal nanoparticles to either oxide or composite (ceramic and metal, cermet) anodes can substantially enhance catalytic activity. Most such studies again address hydrocarbon utilization,[10–13] but enhancements are often observed even for hydrogen electro-oxidation.[14,15] These parallel observations suggest an anode that combines a high surface-area, nanostructured ceria with metal nanoparticle catalysts will maximize active site densities of both types (*i.e.*, both metal catalyzed and oxide catalyzed) and result in extremely high activity. A meaningful role for isolated metal catalyst particles, as envisioned in such a structure, is in principle only feasible in connection with a mixed ionic and electronic conductor (MIEC) such as ceria is under the reducing conditions of the anode because the mixed conductivity provides a pathway for electrons to travel from the catalyst particle site to the macroscale current collector. A purely ionic conductor, in contrast, would require a continuous (but porous) coating of the nanoparticle phase,[16] an arrangement that can readily lead to sintering and loss of nanostructure.

As noted by Jiang,[16] the majority of fuel cell electrodes containing nanoparticle catalysts are prepared by wet impregnation of the electrode scaffold synthesized at the high temperatures typical of ceramics processing. While infiltration methods are attractive for their low cost and scalability, they require high temperature treatments to decompose the nitrate precursors (typically 600–800 °C), resulting in undesirably large particles, 20–40 nm in diameter. In addition, precise control of metals loading at quantities less than $\sim$0.1 mg cm^{-2} is often challenging, and, where investigated, growth of catalyst particles during fuel cell operation typically results in a measurable degradation of performance. An emerging alternative method relies on exsolution of transition metal elements such as Ru and Ni from oxides when exposed to the high-temperature, reducing conditions of SOFC anodes[17,18] or similarly the cathodes of solid oxide electrolyzer cells (SOECs).[19] The method has the advantage of producing very small catalyst particles (<5 nm) that have the potential to be regenerated through repeated cycles of dissolution and exsolution, but often suffers from the disadvantage of requiring high precious metals loadings to exceed the solubility limit of the host oxide, typically a perovskite.

In this work, we report the fabrication and characterization of ceria-based SOFC anodes that incorporate precisely the desired features of (i) nanostructured ceria, with inherently high activity for fuel electro-oxidation, and (ii) nanoparticle metals, which further enhance catalytic activity. We utilize pulsed laser deposition to create $Sm_{0.2}Ce_{0.8}O_{2-\delta}$ (SDC) films with highly porous and vertically-oriented morphology to serve as the scaffolding for stabilizing metal nanoparticles and as the mixed ionic and electronic transport pathway to and from the reaction sites. This strategy builds on our earlier study in which it was shown that such SDC films are inherently active for hydrogen electro-oxidation with an activity that monotonically increases with film thickness, indicating that electron or gas transport are not rate-limiting for films as thick as 11 μm, despite the lack of a percolating metal phase and a rather small pore size.[9] This observation implies, as concluded in that earlier work, that the surface reaction step is rate-limiting. Here, metal nanoparticles are applied by sputtering so as to assure fine control over catalyst quantities even at extremely low loadings.

2. Experimental procedures

Two types of electrochemical cell configurations were employed. In the first type, used for the majority of the experiments, patterned Pt current collectors were formed on YSZ (100) single crystal substrates and columnar SDC films were grown over the pattern. The current collector consisted of 5 μm Pt strips spaced 35 μm apart applied by metal liftoff photolithography to the 10 × 10 × 0.5 mm^3 $Y_{0.16}Zr_{0.84}O_{1.92}$ (YSZ) (MTI Corp.) substrates.[8] Pt was selected because of its stability under the high temperature conditions of the subsequent oxide deposition step. The porous SDC ($Sm_{0.2}Ce_{0.8}O_{2-\delta}$) films were prepared by pulsed-laser deposition (PLD, Neocera, with Coherent 102 KrF 248 nm excimer laser, $\sim$2 J cm^{-2}, 20 Hz) from an oxide target of the same composition. The deposition temperature and atmosphere were 650 °C and 100 mTorr O_2, respectively, conditions found to yield porous (rather than dense) films with a vertically oriented morphology.[8,9] Using a total deposition time of 125 min, films of $\sim$2.5 μm in thickness were obtained.

Metals (Pt, Co, Ni, Pd, Au, or Cu) were subsequently applied to the SDC films by D.C. magnetron sputtering (AJA International Lesker), operated with a base pressure of 1×10^{-7} Torr, a working pressure of 3 mTorr Ar, and a D.C. plasma power of 150 W. In the case of Pt, the deposition time was varied between 30 and 310 s, equivalent to varying the thickness between 5 and 50 nm (for deposition on a flat surface) and resulting in application of 11 to 107 μg Pt per cm^2. Deposition times for other metals were fixed to yield a total equivalent thickness of 5 nm. Subsequent to sputter-deposition, the films were annealed at 700 °C under static air for 2 h.

In the second type of configuration, used for SIMS depth profile analysis and further investigation of electrochemical behavior, the Pt pattern was omitted and the porous SDC grown directly on the YSZ substrate. In this case, a relatively thick layer of Pt, 61 nm, was applied by D.C. sputtering, creating both the catalyst layer and the current collector. Post deposition, the cell was again annealed at 700 °C (2 h, air), transforming the sputtered Pt into a porous but interconnected metal network.

The microstructure of the resulting films was examined using a Carl Zeiss LEO 1550VP scanning electron microscope (SEM). For high-resolution imaging, diffraction, and local chemical analysis, FEI Tecnai F20 and F30 transmission electron microscopes (TEM), equipped with EDAX energy dispersive spectrometers (EDS) were employed. In this case, two samples were glued together, thinned, dimpled, and milled with Ar ions prior to the TEM cross-sectional observations. Compositional depth profiling was performed using a CAMECA IMS 7f magnetic sector secondary ion mass spectrometer (SIMS) in combination with a Cs^+ ion beam to etch the film material. To probe the depth of possible Pt penetration, a thicker SDC film (4 μm) was investigated, onto which a metal layer 61 nm in effective thickness was applied.

The electrochemical characteristics of symmetric cells (electrode|electrolyte|electrode) were measured by A.C. impedance spectroscopy (Solartron 1260, perturbation voltage of 20 to 80 mV), carried out under controlled temperatures and atmospheres under zero bias. Contact was made to the current collectors using Pt/Ir (ESPI metals) clips; to avoid possible contamination, no metal pastes were employed. The cells were placed inside a continuous-flow alumina tube to which mixtures of H_2 (or CH_4)–H_2O–Ar were delivered *via* digital mass flow controllers, with humidification achieved by passing a portion of the inlet gas through a water bubbler placed inside an isothermal water bath. The total flow rate was kept constant at 100 $cm^3\ min^{-1}$ (standard temperature and pressure) implying a gas velocity of 35.1 cm min^{-1}. Effluent humidity was monitored using a Rotronic Hygroflex capacitive sensor. Impedance measurements were carried out at temperatures between 500 and 650 °C. Data were analyzed using ZView software (Scribner Associates, version 2.9b).

3. Results and discussion

SEM and TEM micrographs of representative SDC films prepared by PLD are shown in Fig. 1. Consistent with earlier studies, under the optimized pressure of 100 mTorr the oxide grows in the form of vertically-aligned square columns with high surface roughness.[8,9] Deposition under lower oxygen pressures (a few mTorr) led to dense films,[8] whereas growth at higher pressures (~200 mTorr) led to random, disordered microstructures. Based on BET surface area measurements carried out in our previous study of such films,[9] the present 2.5 μm thick films are estimated to have a specific surface area of ~20 $m^2\ g^{-1}$ and an enhancement factor of the surface area (true surface area per unit projected electrolyte area) of ~230. The feature sizes of the structure, both column diameter and spacing between columns, increase with SDC column height, but nevertheless remain nanoscale. The TEM cross-sectional image, Fig. 1c, collected from a position close to the top of the film, reveals an intercolumn spacing of less than 20 nm and a column diameter of ~120 nm.

The morphology of the sputtered Pt layers after annealing is shown in the SEM images of Fig. 2. With increasing Pt thickness from 5 nm to 50 nm, the Pt morphology changes from largely isolated particles to a highly porous, interconnected network. The SIMS depth profiling results, Fig. 3, moreover reveal that Pt is present throughout the entirety of the film, that the amount monotonically decreases with penetration depth, and, further,

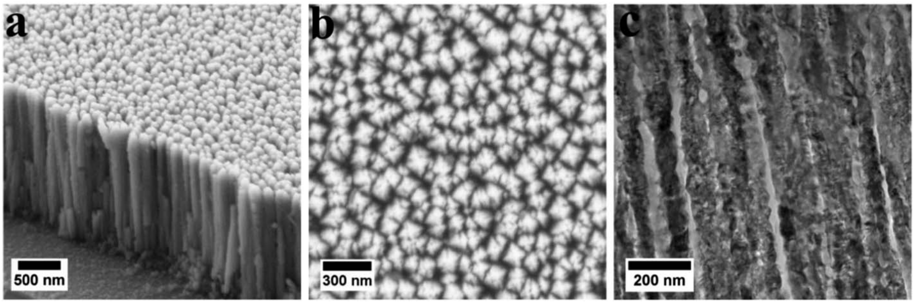

Fig. 1 SEM and TEM micrographs of the porous columnar SDC films prepared by PLD in 100 mTorr O_2 at 650 °C prior to metal deposition. (a) SEM image (cross-sectional view after tilting the sample by 45°). (b) SEM image (top view). (c) TEM image (cross-sectional view), indicating vertical pore-channels with a width of less than 20 nm.

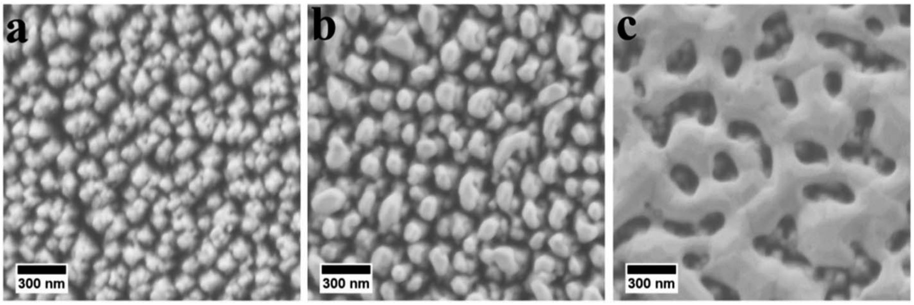

Fig. 2 SEM micrographs of the sputtered Pt layer onto the porous columnar SDC films after annealing at 700 °C (2 h, air). With increasing Pt thickness from 5 nm (a) to 17 nm (b) and 50 nm (c), the Pt morphology changes from largely isolated particles to a highly porous, interconnected network.

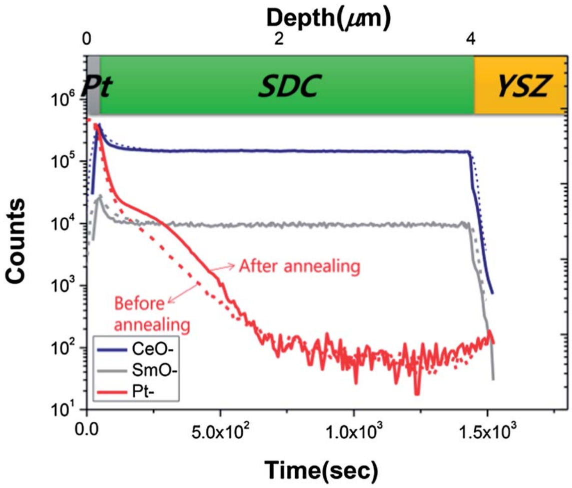

Fig. 3 Depth profile of Pt (red), Ce (blue), and Sm (gray), obtained by SIMS analysis. Substantial amounts of elemental Pt are detected even deeper than 1 μm from the top surface. The effect of annealing at 700 °C (2 h, air) on the depth profile of each element is shown (dotted line: before annealing, solid line: after annealing).

that Pt penetration into the film increases slightly upon heat treatment. The Pt composition profile is generally consistent with the line-of-sight deposition achieved by sputtering, which typically does not permit deep penetration of depositing materials into narrow channels.[20] Here, despite the 120 : 1 aspect ratio, the slight penetration in addition to the high temperature mobility results in the detectable presence of Pt throughout the first 2 μm of film, and its presence is even suggested at the SDC–YSZ interface. The SIMS compositional measurement further shows the Sm : Ce ratio to be relatively uniform over the thickness of the film.

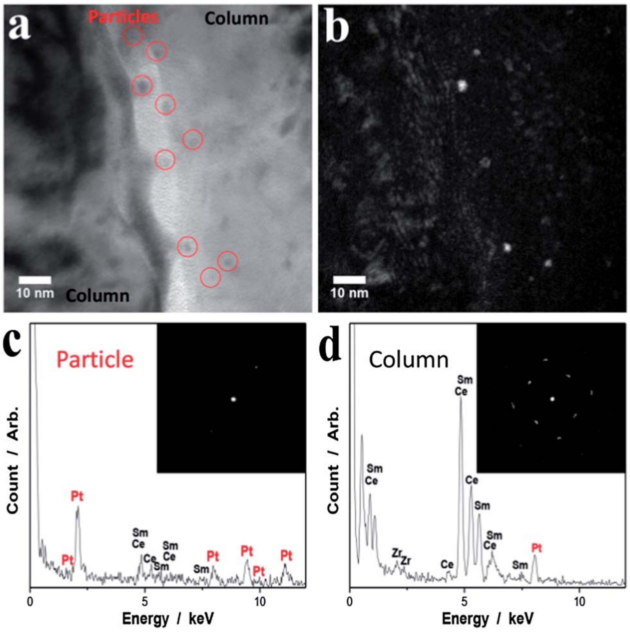

Fig. 4 Bright field (a) and dark field (b) TEM images of the Pt decorated, columnar SDC film after annealing at 650 °C under wet H_2 atmospheres for 100 h. Pt nanoparticles with a diameter of 3–5 nm are highlighted with red circles. Energy Dispersive X-ray Spectroscopy (EDS) and Selected Area Diffraction (SAD, insert) obtained from Pt nanoparticle (c) and SDC column (d).

TEM images of the Pt sputtered films were collected after the completion of the 100 h high-temperature (650 °C) electrochemical measurement under humidified hydrogen (described below). The images directly reveal the presence of Pt nanoparticles on the SDC columns, Fig. 4. Specifically, slightly darker spots in the bright field image, Fig. 4a, are identified as the Pt particles on the basis of the dark field image, Fig. 4b, which reveals the presence of bright spots at positions corresponding to the dark spots in the former. In addition, Selected Area Diffraction (SAD) analysis and Energy Dispersive X-ray Spectroscopy (EDS) (Fig. 4c and d) are consistent with the identification of the ceria and Pt regions. The Pt particles are found to be around 3–5 nm in diameter, the range in which Pt particles are known to display high electro-catalytic activity for low temperature fuel cells such as Polymer Electrolyte Membrane Fuel Cells (PEMFCs) and Phosphoric Acid Fuel Cells (PAFCs).[21] The retention of such small Pt particles after prolonged exposure to aggressive conditions suggests that the highly corrugated columnar structure of the SDC films, in combination with the low overall number density of particles, plays a significant role in stabilizing the metal nanoparticles. Such behavior would not be expected for a high density of particles deposited on a flat oxide surface, despite what is believed to be the inherent stabilizing effect of ceria as a support for catalytic nanoparticles.[22] For example, Rh nanoparticles deposited on flat, dense ceria films with an interparticle spacing of 6 nm show a 50% increase in particle diameter (from 23 to 33 nm) upon exposure to electrochemical perturbations under humidified H_2 at temperatures of 500–650 °C over a period of just 24 h.[14]

Selected electrochemical results obtained at 650 °C are presented in Fig. 5. From the samples with the first type of configuration (the embedded Pt current collector), the raw spectra, Fig. 5a, generally exhibited an offset resistance (R_{off}) at high frequency, evident as a displacement of the data along the real axis, and two adjacent semicircles. In contrast, samples of the second type (top current collector) showed an offset resistance and only a single semicircle at lower frequency, Fig. 5b. The offset resistance from both types of cells is readily attributed to the sum of the YSZ bulk and the Pt sheet resistance. Therefore, for easy interpretation, it is subtracted from the data and omitted from the presented spectra. The high frequency arc of the embedded current collector geometry has been encountered previously for cells of this configuration and is attributed to electronic current constriction effects,[8,14,23] a phenomenon not of interest for the present study. The low frequency arc, however, displays features similar to that of the arc present in the top current collector geometry, suggesting a similar origin (as discussed further below). The spectra were accordingly analyzed by fitting the parameters of an $R(RQ)(RQ)$ equivalent circuit (embedded current collector) or an $R(RQ)$ circuit (top current collector), where Q is a constant phase element of impedance $Z_Q = 1/Y(i\omega)^n$ (Y and n are constants and ω is frequency), and the resistance and capacitance of the low

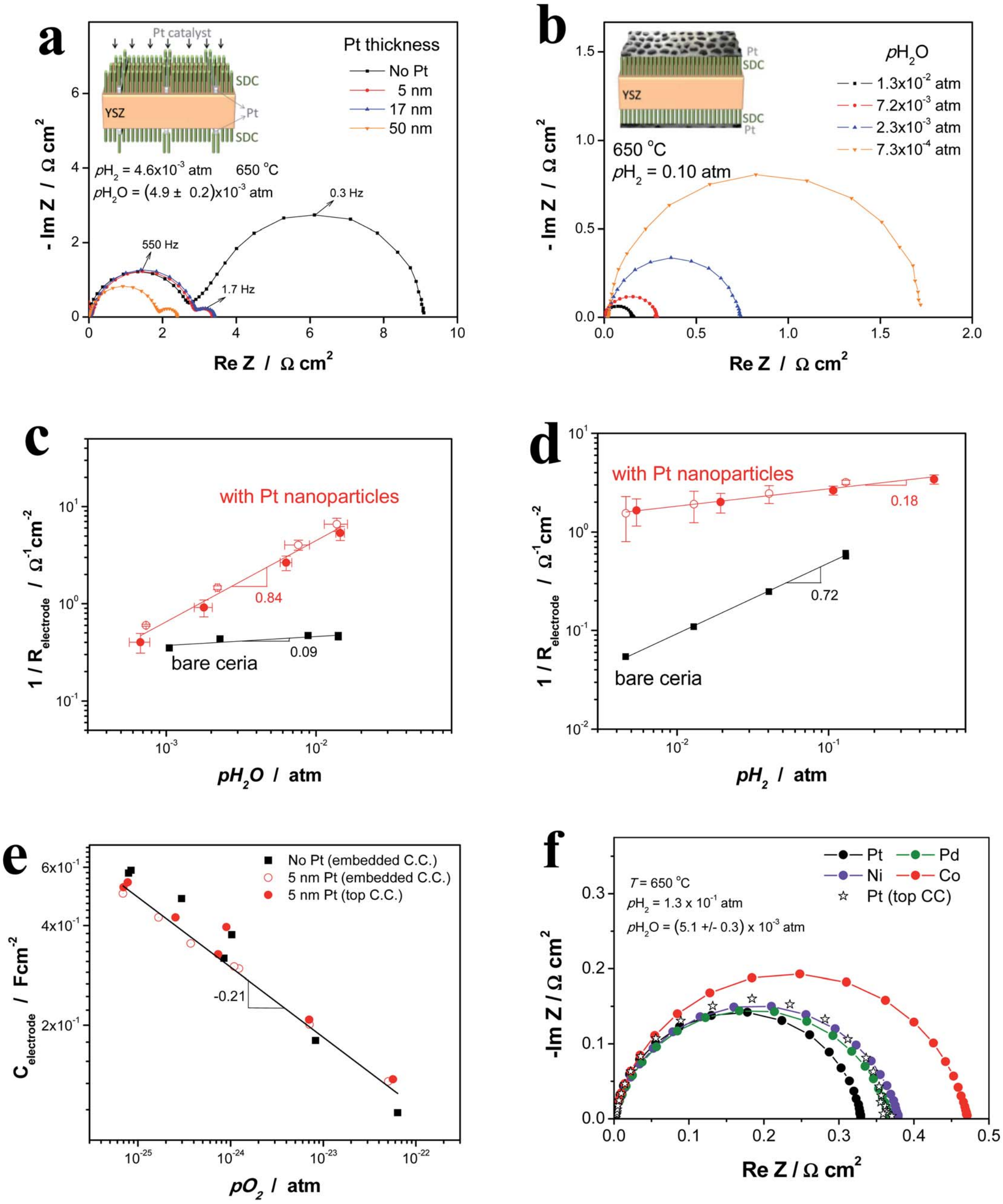

Fig. 5 (a) Typical impedance spectra obtained from SDC|patterned Pt|YSZ(100)|patterned Pt|SDC symmetric cells with/without Pt catalysts. The electrode impedance dramatically decreases after depositing a Pt layer onto the SDC films, while it remains nearly identical regardless of the total amount of Pt deposited by sputtering between 5 nm and 50 nm. (b) Typical impedance spectra obtained from a sputtered Pt|SDC|YSZ(100)|SDC|sputtered Pt symmetric cell as a function of pH_2O. Elimination of electronic current constriction effects eliminates the high frequency arc evident in (a). (c) Double-logarithmic plot of the electrode activity (normalized) *vs.* pH_2O measured at $T = 650$ °C and $pH_2 = 0.05–0.10$ atm. (d) Double-logarithmic plot of the electrode activity (normalized) *vs.* pH_2 measured at $T = 650$ °C and $pH_2O = 0.005$ atm. The electrochemical reaction activities of the two types of cells (embedded current collector and top current collector) were indistinguishable. The errors were determined by six different cells (two embedded current collectors and four top current collectors). (e) Double-logarithmic plot of the electrode capacitance (normalized) *vs.* pO_2 measured at $T = 650$ °C. (f) Comparison of impedance spectra obtained from SDC|patterned Pt|YSZ(100)|patterned Pt|SDC symmetric cells with various catalysts (electronic constriction arc removed).

frequency arc are attributed to the electrochemical reaction. These are denoted $R_{\text{electrode}}$ and $C_{\text{electrode}}$, respectively, and the latter is computed according to $C = (R^{1-n}Q)^{1/n}$, valid for the fits performed here in which n varied between 0.90 and 0.92.

The dependence of $R_{\text{electrode}}$ on gas phase composition is summarized in Fig. 5c and d. Irrespective of the placement of the current collector, the application of Pt nanoparticles both dramatically lowers $R_{\text{electrode}}$ and completely alters the pH_2O and pH_2 dependences. The latter observation suggests a change in mechanism as a result of the presence of the catalyst as discussed further below. Because the response of the catalyzed electrode was found to be insensitive to the amount of Pt present, a result evident from the raw impedance spectra of Fig. 5a, the data for the catalyzed cells with the embedded current collector geometry are averaged in the plots presented in Fig. 5c and d. In addition, four different cells with the top current collector geometry were measured and those results are also averaged here. The identical behaviour for the top and embedded current collector geometries provides further evidence that the low frequency arc in the two configurations arises from the same physical process. The insensitivity of the impedance response to the amount of sputter deposited Pt (embedded current collector geometry) suggests that only a fixed amount of Pt enters the SDC film and contributes to electrocatalysis.

Turning to the capacitive behaviour, we find that $C_{\text{electrode}}$ is very similar for all the cells, irrespective of current collector geometry and the presence or absence of Pt catalyst particles, Fig. 5e. In addition, the slope in the double-logarithmic plot of capacitance *vs.* pO_2 is close the value of -0.25 expected for a capacitance that is dominated by chemical capacitance effects.[24] The result indicates that the entirety of the SDC film responds electrochemically to the voltage perturbation and again gives confidence to the assignment of the origin of the impedance response.

As noted, a substantial mechanistic difference between Pt catalyzed and bare SDC is implied by the distinct differences in dependence of $R_{\text{electrode}}$ for these two classes of anodes on pH_2 and pH_2O. The electrochemical reaction impedance of bare SDC shows high sensitivity to pH_2, but is almost insensitive to variations in pH_2O. This combination suggests that hydrogen electro-oxidation may be rate-limited by elemental processes involving bi-molecular hydrogen species, such as adsorption or dissociation of H_2 on oxide surfaces.[25,26] In addition to lowering the overall electrochemical reaction resistance, application of Pt particles decreases the pH_2 sensitivity of $R_{\text{electrode}}$, suggesting that the catalyst enhances the rates of these steps to such an extent that the rate-determining process may no longer involve the H_2 molecule. This possibility is consistent with observations in the literature that Pt is highly active for H_2 adsorption/dissociation reactions.[27]

Three of the other metals investigated, Ni, Co, and Pd, were found to yield results similar to those of Pt. The electrochemical reaction resistance, $R_{\text{electrode}}$, decreased substantially after application of these metals, although to a lesser degree than Pt, Fig. 5f. In contrast, Au and Cu (not shown) were found to have negligible impact. Furthermore, preliminary investigations of the dependence of $R_{\text{electrode}}$ on gas composition (not shown) suggested that the active catalysts are mechanistically similar to Pt, with high sensitivity to pH_2O and low sensitivity to pH_2, whereas the inactive catalysts retain the pH_2O and pH_2 dependences of bare ceria.

The activity of the metal-decorated SDC films prepared here is substantially greater than that of other ceria–metal composite anodes reported in the literature, Fig. 6. The data from the present work are collected under fuel-cell relevant conditions (98% H_2, 2% H_2O); literature results[15,28–34] correspond to similar but not always identical gas atmospheres. Even in the absence of metal catalysts, the activity of the nanostructured SDC film exceeds that of any previous result reported in the open literature. This behaviour is due in large part to the high specific surface area of the vertical columnar structure in combination with the high inherent surface activity of the oxide, as we have discussed previously.[9] The improved activity afforded by the metal nanoparticles is striking. The electrode polarization resistance attains an unprecedented value of 0.07 Ω cm^2 for Pt-decorated SDC films at 550 °C. The electronic conductivity of SDC under these conditions is 3.7×10^{-2} S cm^{-1} (ref. 35). Thus electronic resistance across the 2.5 μm film contributes just 0.008 Ω cm^2 to the total polarization resistance (after accounting for the ~20% porosity of the films[9]), indicating that, despite the high activity, electron transport has not become a significantly limiting factor. Furthermore, the activation energy associated with the hydrogen-oxidation from the metal-decorated SDC films is exceedingly low, only 0.15 to 0.20 eV, as compared to 0.8–1.4 eV for a typical Ni/YSZ or Ni/SDC anode,

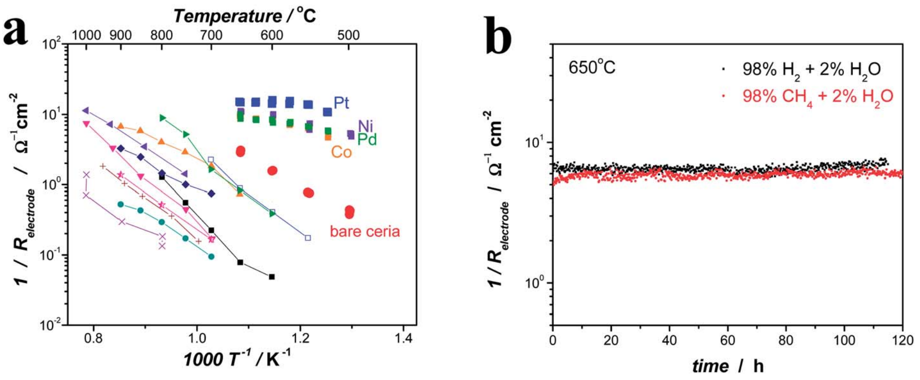

Fig. 6 (a) Arrhenius plot of electrode activity (normalized) for the metal-nanoparticle-decorated SDC thin film in this study. For comparison, the reported electrode activity (normalized) values for typical anodes are also inserted. Ref. 28 (■) = slurry-coated Ni, (□) = slurry-coated Ni/Fe; ref. 29 (▶) = spin-coated Ni/SDC; ref. 15 (▲) = Pd impregnated Ni/GDC; ref. 30 (▼) = sprayed GDC, (◀) = Ni impregnated GDC; ref. 31 (●) = slurry-coated Ni, (♦) = GDC impregnated Ni; ref. 32 (☆ half-filled) = slurry-coated GDC; ref. 33 (+) = slurry-coated Ni/YSZ; ref. 34 (×) = slurry-coated Ni/YSZ. (b) Long term stability of the Pt-nanoparticle-decorated SDC thin film for both H_2 and CH_4 gases, measured at 650 °C, $pH_2 = 0.98$ atm, and $pH_2O = 0.02$ atm.

Fig. 6. A weak temperature-dependence is observed for gas diffusion limited processes, but in the present case, the enhancement of activity upon application of metal nanoparticles, which could only worsen (not improve) gas diffusion kinetics, implies some other factor is rate-limiting, specifically, a surface reaction step. Technologically, the retention of high activity at the low temperatures targeted for lowering overall SOFC costs is particularly attractive.

A significant concern upon utilizing any nanostructured architecture at high temperatures is the possibility of coarsening and loss of the performance advantages afforded by the nanoscale features. Here it is evident, Fig. 6b, that the electrochemical reaction resistance of the Pt-catalyzed ceria is stable for over 100 h of exposure at 650 °C to humid hydrogen and even to humid methane (98% CH_4, 2% H_2O). This stability is further evidence of the absence of significant catalyst particle coarsening and, in the case of methane, of the absence of negative impacts due to carbon deposition. The stability in the latter case is particularly striking as no D.C. current, which could otherwise enhance oxidation of carbon, was drawn. In contrast to the present results, typical SOFCs with Ni/YSZ anodes quickly degrade under open circuit conditions.[7] The similarity of the $R_{\text{electrode}}$ values under H_2 and under CH_4 is also unusual, given the widely appreciated challenges of activating the latter.[7]

It is important to consider whether the strategy reported in this work has suitability as a cost-effective and scalable manufacturing route for commercial SOFC applications. Precious metals such as Pt or Pd cannot be widely used for SOFC electrodes due to their prohibitive cost. However, the total amount of Pt required for achieving high activity in this work is just 10.7 $\mu g\ cm^{-2}$, substantially lower than the typical Pt loadings for PEMFCs[21,36] and thin-film-based micro-fabricated SOFCs.[37] More significantly, if one projects an optimistic but plausible SOFC power output of 3 $W\ cm^{-2}$ at 0.7 V for a fully optimized cell, this quantity of Pt amounts to just 3.6 $\mu g\ W^{-1}$, in turn, contributing (at present prices) less than 0.02 ₵ per W to the raw materials cost. In addition, although PLD has been chosen as the oxide fabrication method for this proof-of-concept study, similar columnar oxide nanostructures can be obtained by more scalable methods such as chemical vapor deposition[38,39] and potentially sputter deposition.[40]

4. Summary

A nanostructured ceria framework has been used as a scaffolding to support metal nanoparticles and create SOFC anodes with unprecedented electrochemical activity for fuel oxidation despite the extremely low precious metals loading. The inherent activity of the ceria structure, which already provides activity exceeding that of all previous reports, is dramatically enhanced in the presence of just 11 $\mu g\ cm^{-2}$ of Pt, Ni, Pd, or Co. In addition, the Pt catalyzed structures have exceptionally high activity for both H_2 and CH_4 electrooxidation, with negligible performance degradation during measurements over periods of over 100 h at 650 °C. The dependence of electrochemical reaction resistance on pH_2 and pH_2O suggests a change in rate-limiting step from one involving dihydrogen molecular species in the absence of Pt to one in which dihydrogen does not play a critical role in the presence of Pt.

The porous, columnar ceria morphology created as the anode scaffold is believed to be desirable as the framework for an SOFC electrode for several reasons. The extreme roughness of the columns is believed to result in large effective interparticle spacings and to also create physical barriers to particle migration and coagulation. These features are essential for maintaining isolated nanoparticles and thus a high number-density of oxide–metal–gas contact points, key sites for electrocatalysis.[14] Moreover, the high specific surface area of the films permits access to the inherently high surface activity of the SDC itself,[8] whereas the linearity of the pore structure may enable easy gas-phase transport of reactant and product species.

In sum, these findings point towards new directions for achieving scalable and high performance SOFCs at reduced operating temperature.

Acknowledgements

This work was supported in part by the Stanford Global Climate Energy Program, by the National Science Foundation under contract number DMR 08-43934, and by Liox, Inc. Additional support was provided by the National Science Foundation through the Caltech Center for the Science and Engineering of Materials, a Materials Research Science and Engineering Center (DMR 05-20565) and by the National Research Foundation of Korea through its support for the Center for Multiscale Energy System, a Global Frontier R&D Program of the Ministry of Science, ICT & Future (2011-0031569).

Notes and references

1 S. M. Haile, *Acta Mater.*, 2003, **51**, 5981–6000.
2 DOE/NETL-2011-1482, February 25, 2011.
3 B. C. H. Steele and A. Heinzel, *Nature*, 2001, **414**, 345–352.
4 Z. Shao and S. M. Haile, *Nature*, 2004, **43**, 170–173.
5 S. Choi, S. Yoo, J. Kim, S. Park, A. Jun, S. Sengodan, J. Kim, J. Shin, H. Y. Jeong, Y. Choi, M. Liu and G. Kim, *Sci. Rep.*, 2013, **3**, 2426.
6 A. Atkinson, S. A. Barnett, R. J. Gorte, J. T. S. Irvine, A. J. McEvoy, M. B. Mogensen, S. Singhal and J. Vohs, *Nat. Mater.*, 2004, **3**, 17–27.
7 S. Mcintosh and R. J. Gorte, *Chem. Rev.*, 2004, **104**, 4845–4865.
8 W. C. Chueh, Y. Hao, W. Jung and S. M. Haile, *Nat. Mater.*, 2012, **11**, 155–161.
9 W. Jung, J. O. Dereux, W. C. Chueh, Y. Hao and S. M. Haile, *Energy Environ. Sci.*, 2012, **5**, 8682–8689.
10 A. Babaei, L. Zhang, E. J. Liu and S. P. Jiang, *Int. J. Hydrogen Energy*, 2012, **37**, 15301–15310.
11 Y. M. Ye, T. M. He, Y. Li, E. H. Tang, T. L. Reitz and S. P. Jiang, *J. Electrochem. Soc.*, 2008, **155**, B811–B818.
12 Z. H. Bi and J. H. Zhu, *J. Power Sources*, 2010, **195**, 3097–3104.

13 G. Kim, G. Corre, J. T. S. Irvine, J. M. Vohs and R. J. Gorte, *Electrochem. Solid-State Lett.*, 2008, **11**, B16–B19.

14 D. A. Boyd, Y. Hao, C. Li, D. G. Goodwin and S. M. Haile, *ACS Nano*, 2013, **7**, 4919–4923.

15 A. Babaei, S. P. Jiang and J. Li, *J. Electrochem. Soc.*, 2009, **156**, B1022–B1029.

16 S. P. Jiang, *Int. J. Hydrogen Energy*, 2012, **37**, 449–470.

17 B. D. Madsen, W. Kobsiriphat, Y. Wang, L. D. Marks and S. A. Barnett, *J. Power Sources*, 2009, **166**, 64–67.

18 D. Neagu, G. Tsekouras, D. N. Miller, H. Menard and J. T. S. Irvine, *Nat. Chem.*, 2013, **5**, 916–923.

19 G. Tsekouras, D. Neagu and J. T. S. Irvine, *Energy Environ. Sci.*, 2013, **6**, 256–266.

20 K. Wasa, I. Kanno and H. Kotera, *Handbook of Sputter Deposition Technology: Fundamentals and Applications for Functional Thin Films, Nano-Materials and MEMS*, William Andrew, 2012.

21 I. EG&G Technical Services, *Fuel Cell Handbook*, 2007.

22 A. Cao, R. Lu and G. Veser, *Phys. Chem. Chem. Phys.*, 2010, **12**, 13499–13510.

23 E. C. Brown, Ph.D. thesis, California Institute of Technology, 2011.

24 W. C. Chueh and S. M. Haile, *Phys. Chem. Chem. Phys.*, 2009, **11**, 8144–8148.

25 W. G. Bessler, M. Vogler, H. Stormer, D. Gerthsen, A. Utz, A. Weber and E. Ivers-Tiffee, *Phys. Chem. Chem. Phys.*, 2010, **12**, 13888–13903.

26 S. Primdahl and M. Mogensen, *Solid State Ionics*, 2002, **152**, 597–608.

27 B. Hammer and J. K. Norskov, *Nature*, 1995, **376**, 238–240.

28 T. Ishihara and H. Zhong, *Scr. Mater.*, 2011, **65**, 108–111.

29 M. Chen, B. H. Kim, Q. Xu and B. G. Ahn, *J. Membr. Sci.*, 2009, **334**, 138–147.

30 S. Primdahl and Y. L. Liu, *J. Electrochem. Soc.*, 2002, **149**, A1466–A1472.

31 S. P. Jiang, S. Zhang, Y. D. Zhen and A. P. Koh, *Electrochem. Solid-State Lett.*, 2004, **7**, A282–A285.

32 T. Nakamura, T. Kobayashi, K. Yashiro, A. Kaimai, T. Otake, K. Sato, J. Mizusaki and T. Kawada, *J. Electrochem. Soc.*, 2008, **155**, B563–B569.

33 X. G. Wang, N. Nakagawa and K. Kato, *J. Electrochem. Soc.*, 2001, **148**, A565–A569.

34 P. Holtappels, I. C. Vinke, L. G. J. de Haart and U. Stimming, *J. Electrochem. Soc.*, 1999, **146**, 2976–2982.

35 W. Lai and S. M. Haile, *J. Am. Ceram. Soc.*, 2005, **88**, 2979–2997.

36 H. A. Gasteiger, S. S. Kocha, B. Sompalli and F. T. Wagner, *Appl. Catal., B*, 2005, **56**, 9–35.

37 H. Huang, M. Nakamura, P. C. Su, R. Fasching, Y. Saito and F. B. Prinz, *J. Electrochem. Soc.*, 2007, **154**, B20–B24.

38 T.-S. Oh, Ph.D. thesis, California Institute of Technology, 2013.

39 T.-S. Oh, D. A. Boyd, D. G. Goodwin and S. M. Haile, Proton conductivity of columnar ceria thin-films grown by chemical vapor deposition, *Phys. Chem. Chem. Phys.*, 2013, **15**, 2466–2472.

40 E. Gourba, P. Briois, A. Ringuedé, M. Cassir and A. Billard, *J. Solid State Electrochem.*, 2004, **8**, 633–637.